



# Regulative electronic redistribution of CoTe<sub>2</sub>/CoP heterointerfaces for accelerating water splitting

Lei Yang<sup>a,b</sup>, Xuejie Cao<sup>b</sup>, Xiaojun Wang<sup>b,c</sup>, Qinglun Wang<sup>b</sup>, Lifang Jiao<sup>b,\*</sup>

<sup>a</sup> Research Center for Intelligent and Wearable Technology, College of Textiles and Clothing, Qingdao University, Qingdao 266071, China

<sup>b</sup> Key Laboratory of Advanced Energy Materials Chemistry (Ministry of Education), College of Chemistry, Nankai University, Tianjin 300071, China

<sup>c</sup> College of Electromechanical Engineering, Shandong Engineering Laboratory for Preparation and Application of High-Performance Carbon-Materials, Qingdao University of Science & Technology, Qingdao 266061, China

## ARTICLE INFO

### Keywords:

Interfacial effects

Electrocatalysts

Electronic redistribution

Hydrogen evolution reaction

## ABSTRACT

The interfacial synergy effect caused by the space charge transfer of heterojunctions can effectively modify the catalytic activity. Herein, a composite heterojunction catalyst of CoTe<sub>2</sub>/CoP with moderate Gibbs free energy of hydrogen adsorption is designed based on interfacial effects driven by work function difference between CoTe<sub>2</sub> and CoP. As expected, CoTe<sub>2</sub>/CoP only needs overpotentials of 80 mV at 10 mA cm<sup>-2</sup> and stability for continuous catalysis at the current density of 100 mA cm<sup>-2</sup> for 20 h in hydrogen evolution reaction (HER). The experimental results and theory calculations identify that the built-in field drives the transfer of electrons from CoTe<sub>2</sub> to CoP at the interface, which realizes electronic redistribution with increased electron density on the Co atoms in CoP and optimizes the adsorption-free energy of the reaction intermediates, thereby, accelerating HER kinetics. Besides, the CoTe<sub>2</sub>/CoP heterostructure also behaves the excellent catalytic activity towards water splitting.

## 1. Introduction

Hydrogen is considered to be the ideal alternative to conventional fossil fuels due to the features of high calorific value, environmental friendliness, and carbon-free. Actuated electrochemical water splitting into hydrogen at the cathode and oxygen at the anode via utilizing intermittent energy sources such as solar and wind power is a promising technology[1–3]. However, the high energy barrier of water electrolysis reactions has hindered the development of this technology. To date, although precious metals such as platinum- and iridium-based catalysts are acknowledged as the best catalysts for the hydrogen evolution reaction (HER) and oxygen evolution reaction (OER), respectively, the characteristics of prohibitive price and inadequate reserves impede the widespread uses[4,5]. Transition metal chalcogenides, especially sulfides, and selenides, have been investigated as electrocatalysts for water splitting due to sufficient active sites and earth abundance[6–8]. Note that tellurides with comparable conductivity, a member of the sulfide family, show inferior catalytic activity towards water splitting because of the inappropriate adsorption capacity for intermediates[9,10]. Generally speaking, the regulation of electronic structure can optimize the intrinsic adsorption characteristics of catalysts[11]. Thus, unremitting efforts are devoted to boosting the metal-telluride intrinsic activity

based on the component-controllable or doping engineering[10,12,13]. Unfortunately, the performance was still unsatisfactory.

Interface engineering is considered an effective strategy to boost catalytic activity due to the influence of complementary advantages of each phase's catalysts in the heterojunction and interfacial synergy effect[14–19]. It is worth noting that the heterojunction contact interface of two-phase materials may lead to the transfer of electrons, which can tailor the electronic structure of activity sites and improve the catalytic performance. For example, Qian's group reported that p-n junctions composed of FeNi-LDH and CoP due to electron transfer and charge separation occurring spontaneously during the formation of the two-phase interface, which synergistically enhanced the OER performance[20]. Sun et al. constructed Mott-Schottky heterostructure catalysts of Mo-MoS<sub>2</sub>, which exhibit excellent HER performance with an overpotential of 138 mV at 10 mA cm<sup>-2</sup> due to optimizing the sulfur sites' electronic structure with interfacial electron redistribution[21]. Chen et al. unveil the enhancement mechanism of HER catalytic activity of Os-OsSe<sub>2</sub> heterostructures, where the built-in electric field drives the transfer of electrons from Os with the over strong  $\Delta G_{H^*}$  to OsSe<sub>2</sub> with the weak  $\Delta G_{H^*}$  to balance the electronic state and optimizes the intrinsic activity of Os sites, the bi-directional optimization of HER performance is realized[22]. Metallic telluride possesses too weak  $\Delta G_{H^*}$ , thus the

\* Corresponding author.

E-mail address: [jiaolf@nankai.edu.cn](mailto:jiaolf@nankai.edu.cn) (L. Jiao).

<https://doi.org/10.1016/j.apcatb.2023.122551>

Received 12 January 2023; Received in revised form 20 February 2023; Accepted 28 February 2023

Available online 2 March 2023

0926-3373/© 2023 Elsevier B.V. All rights reserved.

interfacial coupling between catalysts with strong  $\Delta G_{H^*}$  and metal telluride maybe improve the catalytic performance in theory. Besides, understanding that charge transfer mechanisms affect catalytic activity is significantly important.

Herein, we reported a hybrid composite of  $\text{CoTe}_2/\text{CoP}$  nanowire arrays with heterointerfaces grown on the titanium mesh (Ti mesh), which was via a one-step phosphotellurization method. The obtained  $\text{CoTe}_2/\text{CoP}$  catalysts show outstanding HER and OER performance based on the interfacial effect. In detail, the current density of 10  $\text{mA cm}^{-2}$  is only needed for the overpotential of 80 mV and 260 mV for HER and OER in the alkaline solution, respectively. Furthermore, The  $\text{CoTe}_2/\text{CoP}$  catalysts exhibit favorable stability and mechanical robustness. Density functional theory (DFT) calculations and experimental results reveal that electrons are transferred from  $\text{CoTe}_2$  to CoP for achieving charge balance due to the different work function values, which effectively increase electron density on the Co atoms in CoP in the interface and regulate the electronic structure of the active sites of Co, besides, the  $\text{CoTe}_2/\text{CoP}$  show reduced water adsorption energy and optimized the  $\text{H}^*$  adsorption free energy ( $\Delta G_{H^*}$ ).

## 2. Experimental section

### 2.1. Chemicals

All the chemicals were used as received without further purification. Cobalt nitrate hexahydrate ( $\text{Co}(\text{NO}_3)_2 \cdot 6 \text{H}_2\text{O}$ , Aladdin), ammonium fluoride ( $\text{NH}_4\text{F}$ , Aladdin), urea ( $\text{CO}(\text{NH}_2)_2$ , Aladdin), sodium hypophosphite ( $\text{NaH}_2\text{PO}_2$ , Aladdin), Tellurium (Te, Aladdin), Ti mesh, hydrochloric acid (HCl, Tianjin Chemical Reagent Wholesale Company), absolute ethanol ( $\text{C}_2\text{H}_5\text{OH}$ , Tianjin Chemical Reagent Wholesale Company), and milli-Q ultrapure water ( $18.2 \text{ M}\Omega \cdot \text{cm}^{-1}$ ), acetone ( $\text{C}_3\text{H}_6\text{O}$ ).

### 2.2. Pretreatment of Ti mesh

In order to remove Ti oxides and decontamination, the Ti was submerged in concentrated HCl and  $\text{C}_3\text{H}_6\text{O}$  was ultrasonicated successively for 5 min, respectively. After that, the Ti was in absolute ethanol and ultrapure water several times until the pH is close to 7, successively. Then the Ti mesh was dried in a vacuum.

### 2.3. Synthesis of $\text{CoTe}_2/\text{CoP}$ Heterojunctions on Ti mesh

1 mmol  $\text{Co}(\text{NO}_3)_2 \cdot 6 \text{H}_2\text{O}$ , 4 mmol  $\text{CO}(\text{NH}_2)_2$ , and 1.67 mmol  $\text{NH}_4\text{F}$  were dissolved in 40 mL  $\text{H}_2\text{O}$  and the solution was stirred to be homogeneous. Then the solution and as-treated Ti mesh ( $4 \times 2 \text{ cm}^2$ ) were transferred into a 50 mL Teflon-lined stainless-steel autoclave and sealed in a homogeneous reactor at 120 °C for 6 h. After the reaction and cooling to room temperature, the resulting sample was rinsed with water, and then it was dried in a vacuum at 60 °C for 12 h. Afterward, the  $\text{CoTe}_2/\text{CoP}$  nanowire array was obtained by a phosphotellurization method. 0.4 g  $\text{NaH}_2\text{PO}_2$  and 0.03 g Te powders were placed upstream of the air stream, and the sample ( $1.5 \times 2 \text{ cm}^2$ ) was placed downstream in a porcelain boat. Subsequently, the porcelain boat was calcined at 350 °C for 2 h in a 100 sccm high-purity  $\text{Ar}/\text{H}_2$  atmosphere.

### 2.4. Synthesis of $\text{CoTe}_2$ on Ti mesh

The synthetic procedure is the same as that for  $\text{CoTe}_2/\text{CoP}$  heterojunctions, except for no  $\text{NaH}_2\text{PO}_2$  powders.

### 2.5. Synthesis of CoP on Ti mesh

The synthetic procedure is the same as that for  $\text{CoTe}_2/\text{CoP}$  heterojunctions, except for no -tellurium powders.

## 2.6. Materials characterization

The materials were characterized by using a powder X-ray diffraction (PXRD, Rigaku D/Max-2500) with a  $\text{Cu K}\alpha$  radiation ( $\lambda = 1.5408 \text{ \AA}$ ) source. The microstructure and morphology were detected by field-emission scanning electron microscopy (SEM, JEOL JSM-7500 F) and transmission electron microscopy (TEM, Talos F200X G2, AEMC). The analysis of valence and electronic structure was determined by X-ray photoelectron spectroscopy (XPS, PHI5000 Versaprobe). The X-ray absorption near-edge structure (XANES) experiments were collected at the photoemission end-station at beamline BL10B in the National Synchrotron Radiation Laboratory (NSRL) in Hefei, China. Raman measurements were conducted on a LabRAM HR Evolution microscope (Horiba Jobin Yvon) equipped with a 633 nm laser.

## 2.7. Electrochemical measurements

Electrochemical measurements were conducted on an electrochemical station in a standard three-electrode system. The as-prepared samples were used as working electrodes. The saturated calomel electrode (SCE) and a graphite rod were used as reference and counter electrodes, respectively. The LSV data was recorded for HER and OER with a scan rate of  $5 \text{ mV s}^{-1}$ . Different scanning rates of 10, 20, 40, 60, 80, and 100  $\text{mV s}^{-1}$  of CV cycling in the range of non-faradic districts were performed to evaluate the double layer capacitance. The electrochemical impedance spectroscopy (EIS) measurements were performed at a given potential in the frequency range of  $10^5 \text{ Hz}$  to  $10^{-1} \text{ Hz}$ . Chronoamperometric measurement curves (i-t curves) were carried out at a constant current density to explore the stability. All the potential was calibrated to the reversible hydrogen electrode (vs. RHE) according to the formula ( $E_{\text{vs. RHE}} = E_{\text{vs. SCE}} + E_{\text{SCE}}^0 + 0.059 \text{ pH}$ ).

## 3. Results and discussion

The  $\text{CoTe}_2/\text{CoP}$  catalysts were prepared via the method of a hydrothermal reaction and gas-phase phosphotellurization. The whole process synthesis is schematically illustrated in Fig. 1a and the specific details including compared catalysts are in Experimental Section. The X-ray diffraction (XRD) patterns of  $\text{CoTe}_2/\text{CoP}$  on Ti mesh confirm that the characteristic peaks should be indexed to the CoP phase (PDF#29-0497),  $\text{CoTe}_2$  (PDF#89-2091), and metal Ti, respectively, as shown in Fig. 1b. As well, the  $\text{CoTe}_2/\text{Ti}$  mesh and  $\text{CoP}/\text{Ti}$  mesh are also obtained and the crystalline-phase structures are evidenced by the XRD patterns (Fig. S1 and S2). Scanning electron microscopy (SEM) and transmission electron microscopy (TEM) are used to characterize the morphology. SEM images of  $\text{CoTe}_2/\text{CoP}$  present the cross-linked nanowire array in morphology (Fig. 1c, d), which is consistent with the nanowire morphology of single-phase CoP and  $\text{CoTe}_2$  (Fig. S3). TEM images also show the typical nanowire with a diameter of 150 nm (Fig. 1e). Because of the advantages of nanowire structure,  $\text{CoTe}_2/\text{CoP}$  exhibits hydrophilicity with the test of wettability (Fig. S4), demonstrating the fast mass and charge transfer behavior. As shown in Fig. 1f, the high-resolution TEM images demonstrate a contact interface between two distinct kinds of lattices, where the lattice distance of 0.163 nm and 0.223 nm are attributed to the plane of CoP (020) and  $\text{CoTe}_2$  (121), respectively. On an extended scale, abundant heterointerfaces still exist (Fig. S5). The high-angle annular dark-field scanning TEM (HAADF-STEM) image and energy-dispersive X-ray (EDX) element mapping images illustrate that the elements of Co, P, and Te are uniformly distributed in the  $\text{CoTe}_2/\text{CoP}$  (Fig. 1f). In addition, the Raman spectrum also shows the characteristic peak of Co-P and Co-Te (Fig. S6). The molar ratio of  $\text{CoTe}_2/\text{CoP}$  is about 1:7 based on the inductively coupled plasma (ICP) in Table S1. According to the aforementioned analyses, the heterostructure  $\text{CoTe}_2/\text{CoP}$  with a specific interface was successfully prepared.

X-ray photoelectron spectroscopy (XPS) and synchrotron X-ray

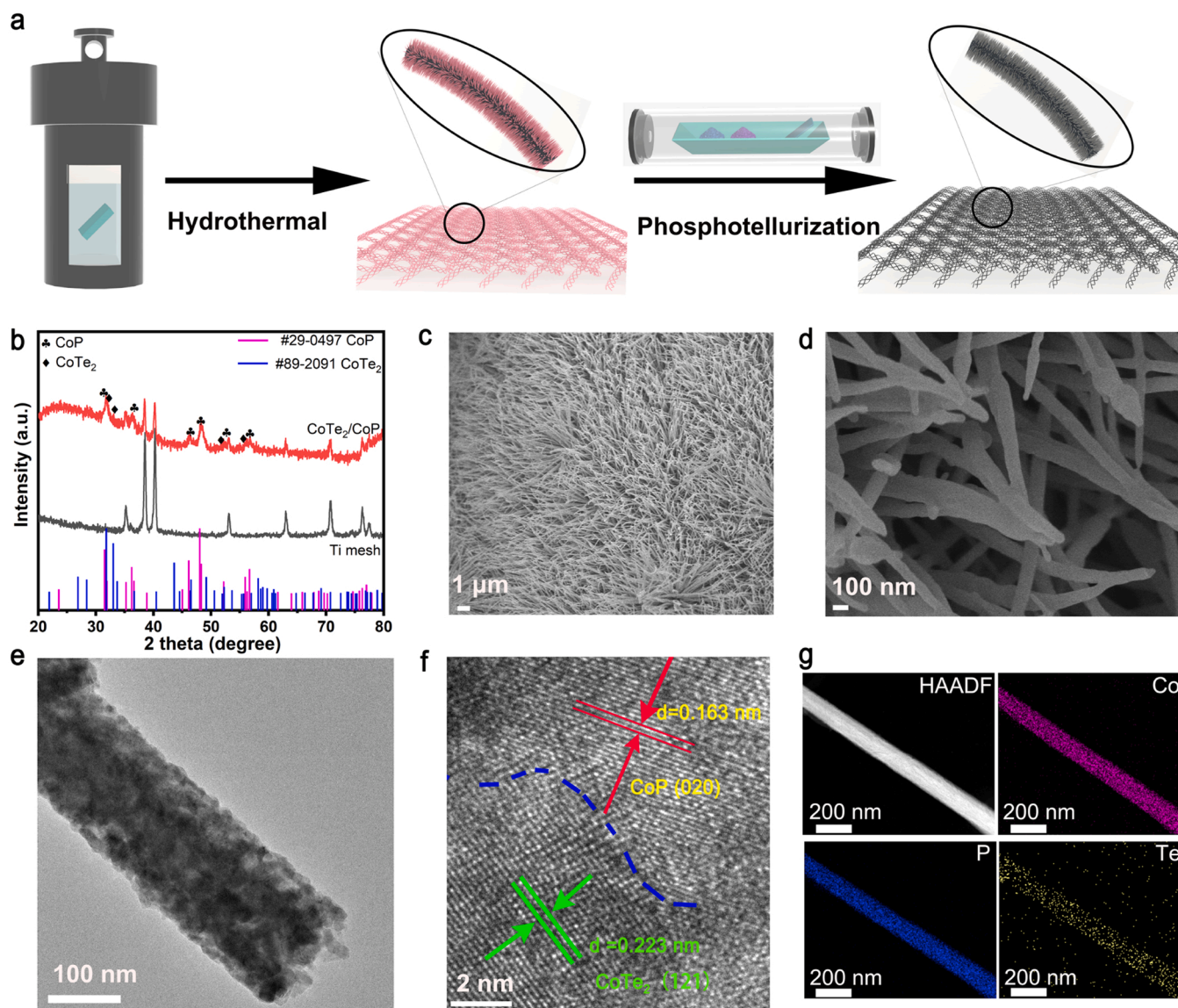


**Fig. 1.** Characterization of CoTe<sub>2</sub>/CoP (a) The schematic diagram for the synthetic route of CoTe<sub>2</sub>/CoP materials on the Ti mesh. (b) The XRD patterns of CoTe<sub>2</sub>/CoP on the Ti mesh. (c,d) SEM images of CoTe<sub>2</sub>/CoP with different magnifications. (e) TEM images of CoTe<sub>2</sub>/CoP. (f) HRTEM images of CoTe<sub>2</sub>/CoP. (g) HAADF-STEM images and EDX mapping.

absorption near-edge structure (XANES) spectroscopy were applied to account for the interfacial effect and chemical states of CoTe<sub>2</sub>/CoP. The XPS survey spectrum of CoTe<sub>2</sub>/CoP suggests the presence of Co, Te, and P elements (Fig. S7), agreeing with the EDX-mapping results. Fig. 2a shows Co 2p high-resolution spectra of CoTe<sub>2</sub>, CoP, and CoTe<sub>2</sub>/CoP. The peak at the binding energy of 779.1 eV in CoP and 778.2 eV in CoTe<sub>2</sub> is owing to the Co-P bond and Co-Te bond, respectively[23]. The other peaks of Co 2p at the higher binding energy (~782.4 eV and 798.5 eV, ~786.6 eV and 803.4 eV) are recognized as oxidation state and satellite peaks of cobalt, respectively[24,25]. The Co 2p peak shows a negative shift (0.5 eV) in CoTe<sub>2</sub>/CoP compared with that of CoP. Meanwhile, the XANES spectroscopy shows Co L-edge with photo energy peaks of L<sub>3</sub> and L<sub>2</sub>, corresponding to the electron transition from 2p to 3d, respectively [26]. Similarly, the peak position at Co L-edge in CoTe<sub>2</sub>/CoP shifted negatively and positively compared to that of CoP and CoTe<sub>2</sub>, respectively (Fig. 2b). The phenomenon of shifting in XPS 2p and L-edge spectra signifies the strong interaction between CoP and CoTe<sub>2</sub>. In the XPS spectrum of Te 3d, the peaks of Te 3d<sub>3/2</sub> (B.E. 583.1 eV) and 3d<sub>5/2</sub> (B.E. 572.8 eV) exhibit a positive shift compared to pure CoTe<sub>2</sub>[27] (Fig. 2c). Conversely, the two peaks at 130.6 eV and 129.7 eV assigned

to P 2p<sub>1/2</sub> and 2p<sub>3/2</sub> negatively shift (0.3 eV) in contrast to pure CoP [28], as shown in Fig. 2d. Overall, all these results indicate that the electrons transfer from CoTe<sub>2</sub> to CoP and increased electron density on the Co atoms in CoP in the interface, which can lead to electron redistribution[29].

The HER performance of heterostructure CoTe<sub>2</sub>/CoP was firstly evaluated with a three-electrode system in the 1 M KOH electrolytes. In addition, the control catalysts of CoP, CoTe<sub>2</sub>, commercial Pt/C, and Ti mesh were also explored. Detailed test steps are shown in Experimental Section. The linear sweep voltammograms (LSV) curves of CoTe<sub>2</sub>/CoP in Fig. 3a show significantly enhanced HER activity over that of CoP, CoTe<sub>2</sub>, and Ti mesh. Therein, CoTe<sub>2</sub>/CoP needs an overpotential of 80 mV and 148 mV to achieve the current density of 10 mA cm<sup>-2</sup> and 100 mA cm<sup>-2</sup>, respectively. The overpotential for achieving the same current density in CoTe<sub>2</sub>/CoP catalysts is lower than CoTe<sub>2</sub>, CoP, and other reported catalysts, as summarized in Fig. 3b and Table S2. Tafel-slope tests are used for assessing the kinetics of the electrocatalytic reaction. As shown in Fig. 3c, the derived values of Tafel slopes are 57, 64, and 141 mV/dec for the catalysts of CoTe<sub>2</sub>/CoP, CoP, and CoTe<sub>2</sub>, respectively, meaning that CoTe<sub>2</sub>/CoP behaves with fast reaction



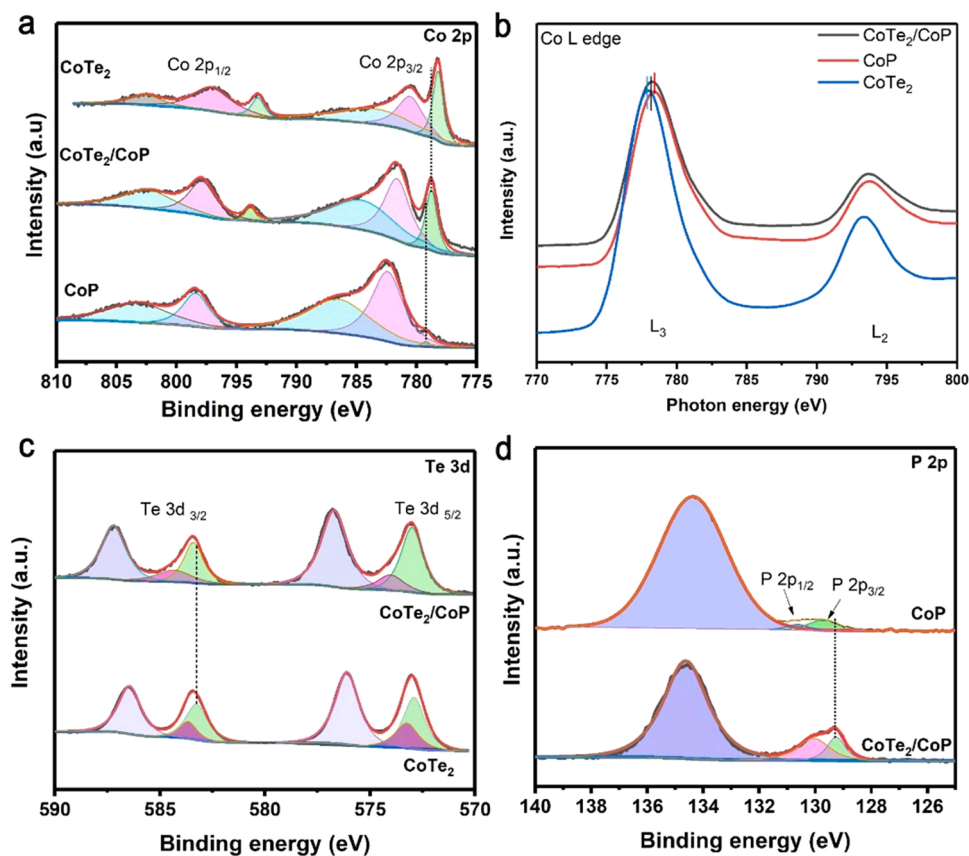


Fig. 2. XPS with peak fitting analysis and XANES spectra of CoTe<sub>2</sub>/CoP (a) Co 2p spectra, (b) Co XANES spectra, (c) Te 3d spectra, (d) P 2p spectra.

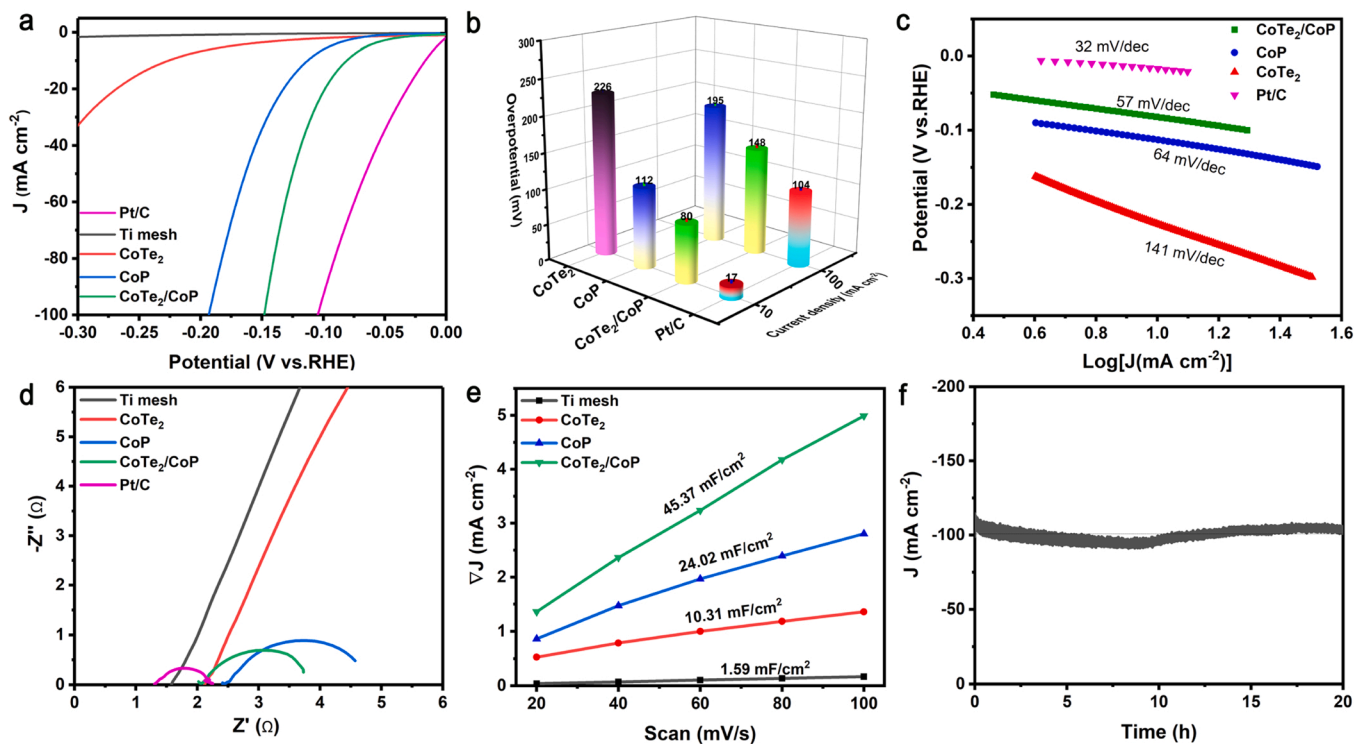


Fig. 3. HER performance of corresponding catalysts (a) LSV curves (b) the overpotential at the current density of 10 and 100 mA cm<sup>-2</sup>, (c) Tafel slope, (d) EIS plots, (e) calculated electrochemical double-layer capacitances, (f) the stability test with  $i$ - $t$  curves.

kinetics. To sum up, the decent HER activity of CoTe<sub>2</sub>/CoP implies the importance of constructing heterointerfaces for boosting the catalytic performance. Furthermore, electrochemical impedance spectroscopy (EIS) in Fig. 3d shows that CoTe<sub>2</sub>/CoP has a smaller radius than that of contrast samples, implying a decreased charge transfer resistance ( $R_{ct}$ ) and a rapid mass/charge transfer process[30,31]. The electrochemical double-layer capacitance ( $C_{dl}$ ), derived from the CV at different scans in the Non-Faraday region (Fig. S8), is reckoned as the assessment of the electrochemically surface area (ECSA). As shown in Fig. 3e, the CoTe<sub>2</sub>/CoP catalysts show much larger  $C_{dl}$  values (45.37 mF/cm<sup>2</sup>) than that of CoP (24.02 mF/cm<sup>2</sup>), CoTe<sub>2</sub> (10.31 mF/cm<sup>2</sup>), and Ti mesh (1.59 mF/cm<sup>2</sup>), implying the more exposed active sites. Besides, the LSV curves with normalization by ECSA exhibit the best HER intrinsic activity compared with control samples (Fig. S9), suggesting that boosting electro-catalytic performance may be attributed to the interface effect of electron transfer[32]. Stability is another important parameter to evaluate the performance of CoTe<sub>2</sub>/CoP catalysts. The potentiostatic method was performed to monitor around the current density of 100 mA cm<sup>-2</sup> in Fig. 3f, which has no apparent floating during the 20-hour continuous HER process. More importantly, CoTe<sub>2</sub>/CoP shows that the crystal structure and morphology of the nanowire array keep unchanged after HER based on characterizations of the XRD (Fig. S10) and SEM (Fig. S11a). Significantly, the obvious interface between CoTe<sub>2</sub> and CoP is well preserved from the HRTEM images (Fig. S11b, c), besides, the chemical states of CoTe<sub>2</sub>/CoP remain almost unchanged after HER electrocatalysis (Fig. S11d-f), which together illustrates the extraordinary durability and interface stability. Therefore, such an outstanding performance offers a bright prospect for designing the heterostructure with an interface effect.

To unveil the relationship between the interface effect and HER catalytic activity at the atomic level, the DFT calculations were constructed. The computational details are given in the Supporting Information. The constructional models of CoTe<sub>2</sub>, CoP, and CoTe<sub>2</sub>/CoP are shown in Fig. S12. Firstly, the deformation charge density of CoTe<sub>2</sub>/CoP displays that CoTe<sub>2</sub> and CoP share the same Co atom in the interface and significant electron transfer occurs at the interface in Fig. 4a. The work function

(WF) value determines the direction and possibility of electron transfer, which describes the driving factor and the balance effect[22,33]. As displayed in Fig. 4b, Fig. S15, and S16, the WF of CoTe<sub>2</sub>, CoP, and CoTe<sub>2</sub>/CoP were calculated and the WF value is 4.68 eV, 5.55 eV, and 4.88 eV, respectively. The different WF signifies that the electrons transfer from high to low levels until the balance. As shown in Fig. 4c, the electrons transfer from CoTe<sub>2</sub> to CoP via an interface until the balance of the systems, which is consistent with the analysis results of XPS and XANES. In addition, benefiting from electron transfer caused by different WF, the density of states (DOS) shows more electrons near the Fermi level compared to pure CoTe<sub>2</sub> and CoP in Fig. 4d, which means higher conductivity and more favorable catalytic activity[22]. Finally, the HER process in an alkaline system involves the following steps: water molecular adsorption/dissociation, and H\* adsorption/desorption[34]. The corresponding adsorption model is shown in Fig. S12-S14. We calculated the energy of each step reaction. The CoTe<sub>2</sub>/CoP has lower water molecular adsorption energy (−0.653 eV) compared with CoTe<sub>2</sub> (−0.379 eV) and CoP (−0.638 eV) in Fig. 4e, signifying that water molecules are more likely to adsorb on the surface of the catalyst of CoTe<sub>2</sub>/CoP and is more conducive to the subsequent reaction. As displayed in Fig. 4f, the CoP shows the smallest water dissociation free energy (0.387 eV) but exhibits the largest H adsorption free energy ( $\Delta G_H = -1.19$  eV), suggesting that H\* is more difficult to desorb. The CoTe<sub>2</sub> displays the largest water dissociation-free energy (1.32 eV) and  $\Delta G_H$  (0.347 eV), indicating the more difficult process of water dissociation. Note that the CoTe<sub>2</sub>/CoP shows moderate water dissociation-free energy of 0.62 eV and  $\Delta G_H$  (−0.158 eV), which illustrates that CoTe<sub>2</sub>/CoP shows better HER performance in thermodynamics. To sum up, the DFT results validate the space charge effect drives the electron transfer at the interface of CoTe<sub>2</sub>/CoP, which optimizes the adsorption energy of the intermediate and boosts the electrocatalytic performance of HER.

Encouraged by enhanced HER activity of CoTe<sub>2</sub>/CoP with the interface effect, we also explored the performance towards OER and overall water splitting. As expected, the anode OER catalysts of CoTe<sub>2</sub>/CoP outperformed the pure CoTe<sub>2</sub> and CoP catalysts in Fig. 5a. The overpotential of 260 and 354 mV could drive the current density of 10

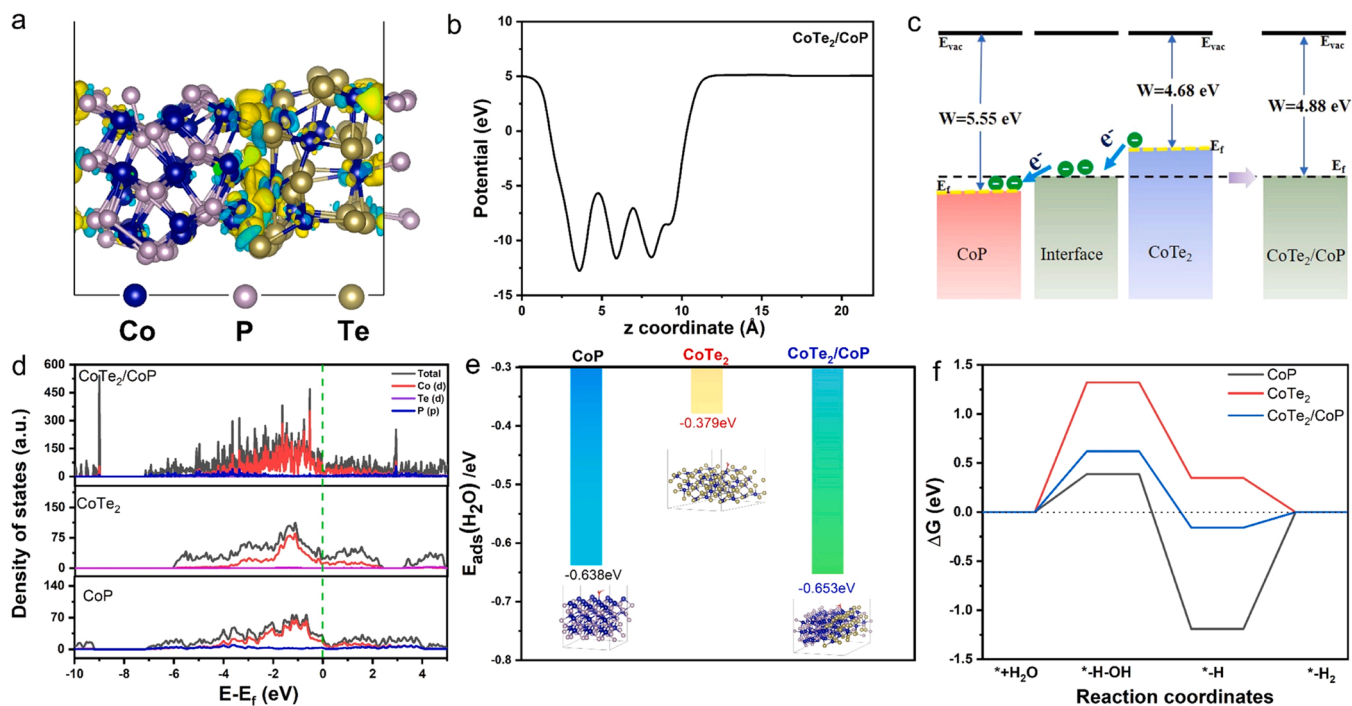
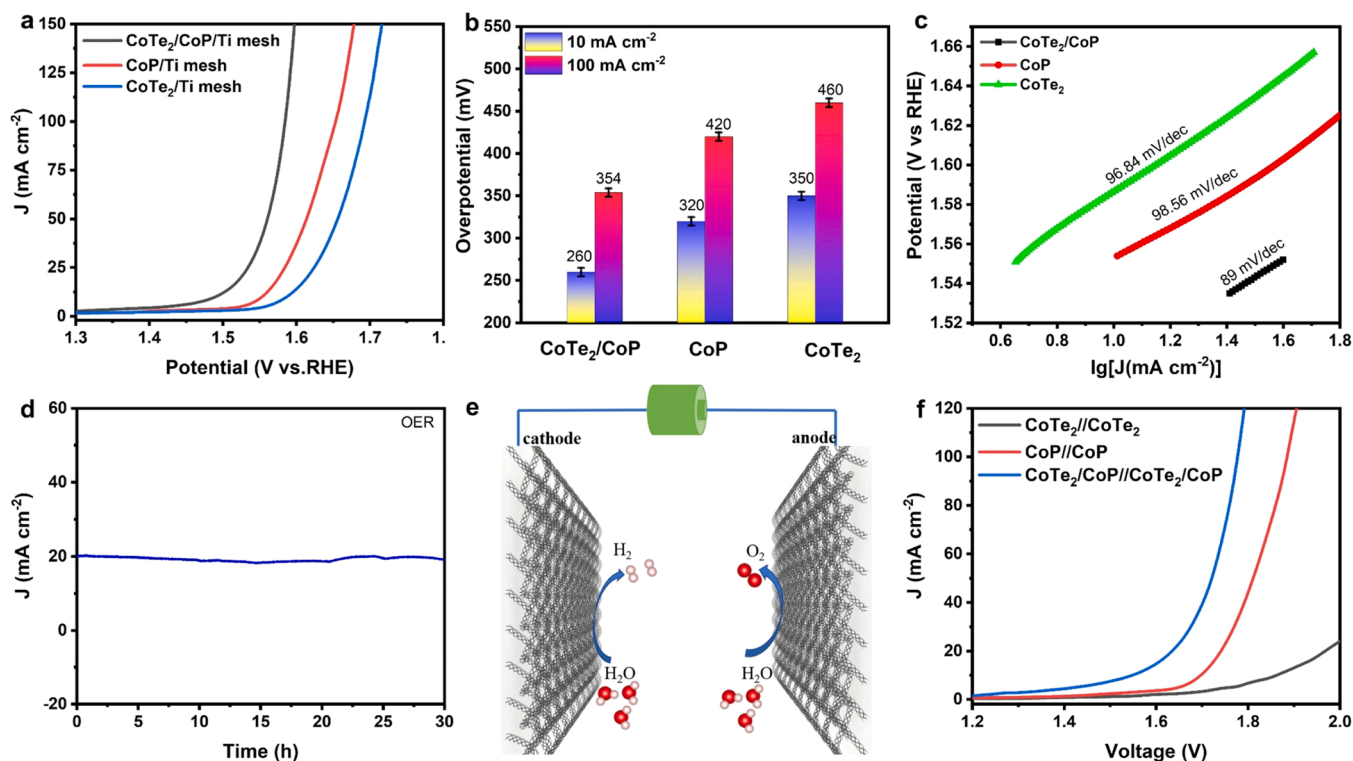


Fig. 4. DFT calculations. (a) Deformation charge density of CoTe<sub>2</sub>/CoP, Isosurface = 0.007 e bohr<sup>-3</sup>. (Yellow means electron accumulation and cyan means electron depletion), (b) The WF of CoTe<sub>2</sub>/CoP, (c) Schematic diagram of the work function and electron transfer, (d) calculated DOS, (e) water molecular adsorption energy of CoTe<sub>2</sub>/CoP, CoTe<sub>2</sub>, and CoP, (f) the  $\Delta G$  of reaction process for the electrocatalytic HER under alkaline conditions and  $\Delta G_{H^*}$  diagram of samples.



**Fig. 5.** OER and overall water splitting performance. (a) LSV curves of OER, (b) the overpotential at the current density of 10 and 100 mA cm<sup>-2</sup>, (c) Tafel slope, (d) i-t curves of CoTe<sub>2</sub>/CoP, (e) graphic of two-electrode electrolyzer, (f) polarization curves of the two-electrode electrolyzer.

and 100 mA cm<sup>-2</sup> based on CoTe<sub>2</sub>/CoP catalysts, respectively, which is lower than CoP (320 and 420 mV) and CoTe<sub>2</sub> (350 and 460 mV) as displayed in Fig. 5b. Similarly, the smaller Tafel slope of CoTe<sub>2</sub>/CoP (89 mV/dec) among the control catalysts implies faster OER kinetics (Fig. 5c). In addition, CoTe<sub>2</sub>/CoP shows superior long-cycle stability with continuous OER for 30 h at the catalytic current density of 20 mA cm<sup>-2</sup>. In order to deeply understand the OER performance of CoTe<sub>2</sub>/CoP, we characterized the catalysts after the OER test. The nanowire morphology was preserved while a rough and incompact surface had been formed (Fig. S17a). Thus, the XPS and Raman spectrum was further employed to explore the surface property. XPS spectrum illustrates that the valence of Co<sup>2+</sup> increases to Co<sup>3+</sup> and forms the CoOOH combined with analysis of the O 2p spectrum and Raman spectrum (Fig. S17a, f). Note that P elements are disappeared and Te is oxidized with a higher valence (Fig. S17 and Table S3). The results indicated that the catalyst was reconstructed and the active species (CoOOH) were generated, which promoted the activity and is consistent with the reported literature [35–37]. Originating from the excellent HER and OER activities of the CoTe<sub>2</sub>/CoP, we assembly the two-electrode electrolyzer to achieve overall water splitting in an alkaline solution, as displayed in Fig. 5e. The LSV curves show the CoTe<sub>2</sub>/CoP behaves the satisfactory activity towards overall water splitting with the obtained current density of 10 mA cm<sup>-2</sup> for the voltage of 1.55 V in Fig. 5f. Furthermore, the CoTe<sub>2</sub>/CoP exhibits relatively stability at the catalyzing current density of 50 mA cm<sup>-2</sup> in Fig. S18.

#### 4. Conclusion

In summary, the bifunctional catalysts of CoTe<sub>2</sub>/CoP were fabricated for water splitting via a facile phosphotellurization method. Benefiting from the interface effect between CoTe<sub>2</sub> and CoP, the electron-redistribution CoTe<sub>2</sub>/CoP behaves the intriguing HER activity and stability, which needs an overpotential of 80 mV for 10 mA cm<sup>-2</sup> and a long stable cycle has been achieved for the current density of 100 mA cm<sup>-2</sup> in an alkaline solution. DFT calculations and detailed

experimental results illustrate that different work functions drive electron transfer from CoTe<sub>2</sub> to CoP at the contact interface and achieve increased electron density on the Co atoms in CoP at the interface of heterojunctions, which optimizes the adsorption-free energy of active species and boosts the HER activity. Meanwhile, CoTe<sub>2</sub>/CoP catalysts also present outstanding performance of overall water splitting. This work not only can provide the strategy for designing high-efficient catalysts based on interface effect but also understand the regulating mechanism of the electronic structure in fields of electrocatalysis water splitting and beyond.

#### CRediT authorship contribution statement

**Lei Yang:** Methodology, Investigation, Writing – original draft. **Xuejie Cao:** Investigation, Validation. **Xiaojun Wang:** Visualization, Software. **Qinglun Wang:** review. **Lifang Jiao:** Supervision, Writing – review & editing.

#### Declaration of Competing Interest

The authors declare that they have no known competing financial interests or personal relationships that could have appeared to influence the work reported in this paper.

#### Data Availability

Data will be made available on request.

#### Acknowledgements

This work was financially supported by the National Natural Science Foundation of China (52025013, 22121005, 22005167), the Fundamental Research Funds for the Central Universities, and the Shandong Provincial Natural Science Foundation of China (ZR2022QE003, ZR2020QB125). The authors thank the Photoemission Endstations

(BL10B) in National Synchrotron Radiation Laboratory (NSRL) for help in characterizations.

## Appendix A. Supporting information

Supplementary data associated with this article can be found in the online version at [doi:10.1016/j.apcatb.2023.122551](https://doi.org/10.1016/j.apcatb.2023.122551).

## References

- Q. Xu, J. Zhang, H. Zhang, L. Zhang, L. Chen, Y. Hu, H. Jiang, C. Li, Atomic heterointerface engineering overcomes the activity limitation of electrocatalysts and promises highly-efficient alkaline water splitting, *Energy Environ. Sci.* 14 (2021) 5228–5259.
- J. Zhu, L. Hu, P. Zhao, L.Y.S. Lee, K.Y. Wong, Recent advances in electrocatalytic hydrogen evolution using nanoparticles, *Chem. Rev.* 120 (2020) 851–918.
- X. Gao, X. Liu, W. Zang, H. Dong, Y. Pang, Z. Kou, P. Wang, Z. Pan, S. Wei, S. Mu, John Wang, Synergizing in-grown Ni<sub>3</sub>N/Ni heterostructured core and ultrathin Ni<sub>3</sub>N surface shell enables self-adaptive surface reconfiguration and efficient oxygen evolution reaction, *Nano Energy* 78 (2020), 105355.
- Y. Luo, S. Zhang, H. Pan, S. Xiao, Z. Guo, L. Tang, U. Khan, B.F. Ding, M. Li, Z. Cai, Y. Zhao, W. Lv, Q. Feng, X. Zou, J. Lin, H.M. Cheng, B. Liu, Unsaturated single atoms on monolayer transition metal dichalcogenides for ultrafast hydrogen evolution, *ACS Nano* 14 (2020) 767–776.
- Q. Lin, D. Guo, L. Zhou, L. Yang, H. Jin, J. Li, G. Fang, X. Chen, S. Wang, Tuning the interface of Co<sub>1-x</sub>S/Co(OH)F by atomic replacement strategy toward high-performance electrocatalytic oxygen evolution, *ACS Nano* 16 (2022) 15460–15470.
- H. Jin, X. Wang, C. Tang, A. Vasileff, L. Li, A. Slattery, S.Z. Qiao, Stable and highly efficient hydrogen evolution from seawater enabled by an unsaturated nickel surface nitride, *Adv. Mater.* 33 (2021), 2007508.
- Y. Wang, X. Li, M. Zhang, Y. Zhou, D. Rao, C. Zhong, J. Zhang, X. Han, W. Hu, Y. Zhang, K. Zaghbi, Y. Wang, Y. Deng, Lattice-strain engineering of homogeneous NiSe<sub>0.5</sub>Se<sub>0.5</sub> core-shell nanostructure as a highly efficient and robust electrocatalyst for overall water splitting, *Adv. Mater.* 32 (2020), 2000231.
- L. Zhang, Z. Wang, J. Qiu, Energy-saving hydrogen production by seawater electrolysis coupling sulfon degradation, *Adv. Mater.* 34 (2022), 2109321.
- J. Wang, L. Han, B. Huang, Q. Shao, H.L. Xin, X. Huang, Amorphization activated ruthenium-tellurium nanorods for efficient water splitting, *Nat. Commun.* 10 (2019) 5692.
- H. Wang, Y. Wang, L. Tan, L. Fang, X. Yang, Z. Huang, J. Li, H. Zhang, Y. Wang, Component-controllable cobalt telluride nanoparticles encapsulated in nitrogen-doped carbon frameworks for efficient hydrogen evolution in alkaline conditions, *Appl. Catal. B: Environ.* 244 (2019) 568–575.
- Y. Zhou, J. Zhang, E. Song, J. Lin, J. Zhou, K. Suenaga, W. Zhou, Z. Liu, J. Liu, J. Lou, H.J. Fan, Enhanced performance of in-plane transition metal dichalcogenides monolayers by configuring local atomic structures, *Nat. Commun.* 11 (2020) 2253.
- U.N. Pan, D.R. Paudel, A. Kumar Das, T.I. Singh, N.H. Kim, J.H. Lee, Ni-nanoclusters hybridized 1T–Mn–VTe<sub>2</sub> mesoporous nanosheets for ultra-low potential water splitting, *Appl. Catal. B: Environ.* 301 (2022), 120780.
- Q. Wang, K. Cui, J. Li, Y. Wu, Y. Yang, X. Zhou, G. Ma, Z. Yang, Z. Lei, S. Ren, Phosphorus-doped CoTe<sub>2</sub>/C nanoparticles create new Co-P active sites to promote the hydrogen evolution reaction, *Nanoscale* 12 (2020) 9171–9177.
- L. Yang, L. Huang, Y. Yao, L. Jiao, In-situ construction of lattice-matching NiP<sub>2</sub>/NiSe<sub>2</sub> heterointerfaces with electron redistribution for boosting overall water splitting, *Appl. Catal. B: Environ.* 282 (2021), 119584.
- J. Chen, C. Chen, M. Qin, B. Li, B. Lin, Q. Mao, H. Yang, B. Liu, Y. Wang, Reversible hydrogen spillover in Ru-WO<sub>3-x</sub> enhances hydrogen evolution activity in neutral pH water splitting, *Nat. Commun.* 13 (2022) 5382.
- H. Fu, M. Zhou, P. Liu, P. Liu, H. Yin, K. Sun, H. Yang, M. Al-Mamun, P. Hu, H. Wang, H. Zhao, Hydrogen spillover-bridged volmer/tafel processes enabling ampere-level current density alkaline hydrogen evolution reaction under low overpotential, *J. Am. Chem. Soc.* 144 (2022) 6028–6039.
- L. Yuan, S. Liu, S. Xu, X. Yang, J. Bian, C. Lv, Z. Yu, T. He, Z. Huang, D. W. Boukhvalov, C. Cheng, Y. Huang, C. Zhang, Modulation of Volmer step for efficient alkaline water splitting implemented by titanium oxide promoting surface reconstruction of cobalt carbonate hydroxide, *Nano Energy* 82 (2021), 105732.
- Y. Liu, S. Jiang, S. Li, L. Zhou, Z. Li, J. Li, M. Shao, Interface engineering of (Ni, Fe) S<sub>2</sub>/MoS<sub>2</sub> heterostructures for synergetic electrochemical water splitting, *Appl. Catal. B: Environ.* 247 (2019) 107–114.
- X. Fan, C. Liu, M. Wu, B. Gao, L. Zheng, Y. Zhang, H. Zhang, Q. Gao, X. Cao, Y. Tang, Synergistic effect of dual active sites over Ru/ $\alpha$ -MoC for accelerating alkaline hydrogen evolution reaction, *Appl. Catal. B: Environ.* 318 (2022), 121867.
- K. He, T. Tadesse Tsega, X. Liu, J. Zai, X. Li, X. Liu, W. Li, N. Ali, X. Qian, Utilizing the space-charge region of the FeNi-LDH/CoP p-n junction to promote performance in oxygen evolution electrocatalysis, *Angew. Chem., Int. Ed.* 58 (2019) 11903–11909.
- Z. Sun, L. Lin, M. Yuan, H. Yao, Y. Deng, B. Huang, H. Li, G. Sun, J. Zhu, Mott-Schottky heterostructure induce the interfacial electron redistribution of MoS<sub>2</sub> for boosting pH-universal hydrogen evolution with Pt-like activity, *Nano Energy* 101 (2022), 107563.
- D. Chen, R. Lu, R. Yu, Y. Dai, H. Zhao, D. Wu, P. Wang, J. Zhu, Z. Pu, L. Chen, J. Yu, S. Mu, Work-function-induced Interfacial Built-in Electric Fields in Os-OsSe<sub>2</sub> Heterostructures for Active Acidic and Alkaline Hydrogen Evolution, *Angew. Chem., Int. Ed.* 61 (2022), 202208642.
- Z. Chen, M. Chen, X. Yan, H. Jia, B. Fei, Y. Ha, H. Qing, H. Yang, M. Liu, R. Wu, Vacancy occupation-driven polymorphic transformation in cobalt ditelluride for boosted oxygen evolution reaction, *ACS Nano* 14 (2020) 6968–6979.
- L. Jiang, Y. Huang, Y. Zou, C. Meng, Y. Xiao, H. Liu, J. Wang, Boosting the stability of oxygen vacancies in  $\alpha$ -Co(OH)<sub>2</sub> nanosheets with coordination polyhedrons as rivets for high-performance alkaline hydrogen evolution electrocatalyst, *Adv. Energy Mater.* (2022), 2202351.
- Z. Li, W. Wang, Q. Qian, Y. Zhu, Y. Feng, Y. Zhang, H. Zhang, M. Cheng, G. Zhang, Magic hybrid structure as multifunctional electrocatalyst surpassing benchmark Pt/C enables practical hydrazine fuel cell integrated with energy-saving H<sub>2</sub> production, *eScience* 2 (2022) 416–427.
- Y. Wu, X. Liu, D. Han, X. Song, L. Shi, Y. Song, S. Niu, Y. Xie, J. Cai, S. Wu, J. Kang, J. Zhou, Z. Chen, X. Zheng, X. Xiang, G. Wang, Electron density modulation of NiCo<sub>2</sub>S<sub>4</sub> nanowires by nitrogen incorporation for highly efficient hydrogen evolution catalysis, *Nat. Commun.* 9 (2018) 1425.
- X. Chia, Z. Sofer, J. Luxa, M. Pumera, Unconventionally layered CoTe<sub>2</sub> and NiTe<sub>2</sub> as electrocatalysts for hydrogen evolution, *Chemistry* 23 (2017) 11719–11726.
- X. Guo, X. Wan, Q. Liu, Y. Li, W. Li, J. Shui, Phosphated IrMo bimetallic cluster for efficient hydrogen evolution reaction, *eScience* 2 (2022) 304–310.
- L. Yang, R. Liu, L. Jiao, Electronic redistribution: construction and modulation of interface engineering on CoP for enhancing overall water splitting, *Adv. Funct. Mater.* 30 (2020), 1909618.
- F. Gong, M. Liu, S. Ye, L. Gong, G. Zeng, L. Xu, X. Zhang, Y. Zhang, L. Zhou, S. Fang, J. Liu, All-pH stable sandwich-structured MoO<sub>2</sub>/MoS<sub>2</sub>/C hollow nanoreactors for enhanced electrochemical hydrogen evolution, *Adv. Funct. Mater.* 31 (2021), 2101715.
- H. Sun, C. Tian, G. Fan, J. Qi, Z. Liu, Z. Yan, F. Cheng, J. Chen, C. Li, M. Du, Boosting activity on Co<sub>4</sub>N porous nanosheet by coupling CeO<sub>2</sub> for efficient electrochemical overall water splitting at high current densities, *Adv. Funct. Mater.* 30 (2020), 1910596.
- T. Wang, X. Cao, L. Jiao, Ni<sub>2</sub>P/NiMoP heterostructure as a bifunctional electrocatalyst for energy-saving hydrogen production, *eScience* 1 (2021) 69–74.
- M. Gu, L. Jiang, S. Zhao, H. Wang, M. Lin, X. Deng, X. Huang, A. Gao, X. Liu, P. Sun, X. Zhang, Deciphering the space charge effect of the p-n junction between copper sulfides and molybdenum selenides for efficient water electrolysis in a wide pH range, *ACS Nano* 16 (2022) 15425–15439.
- S. Zhou, H. Jang, Q. Qin, L. Hou, M.G. Kim, S. Liu, X. Liu, J. Cho, Boosting hydrogen evolution reaction by phase engineering and phosphorus doping on Ru/P-TiO<sub>2</sub>, *Angew. Chem., Int. Ed.* (2022), 202212196.
- L. Yang, H. Qin, Z. Dong, T. Wang, G. Wang, L. Jiao, Metallic S-CoTe with surface reconstruction activated by electrochemical oxidation for oxygen evolution catalysis, *Small* 17 (2021), 2102027.
- H. Sun, J.-M. Yang, J.-G. Li, Z. Li, X. Ao, Y. Liu, Y. Zhang, Y. Li, C. Wang, J. Tang, Synergistic coupling of NiTe nanoarrays with RuO<sub>2</sub> and NiFe-LDH layers for high-efficiency electrochemical-/photovoltage-driven overall water splitting, *Appl. Catal. B: Environ.* 272 (2020), 118988.
- P. Guo, S. Cao, Y. Wang, X. Lu, Y. Zhang, X. Xin, X. Chi, X. Yu, I. Tojiboyev, H. Salari, A.J. Sobrido, M. Titirici, X. Li, Surface self-reconstruction of telluride induced by in-situ cathodic electrochemical activation for enhanced water oxidation performance, *Appl. Catal. B: Environ.* 310 (2022), 121355.